# *Ab initio* model of carrier transport in diamond

M. G. C. Alasio,[1,2] M. Zhu,[1] M. Matsubara,[1] M. Goano,[2] and E. Bellotti[1,3,*]

[1] *ECE, Boston University, 8 Saint Mary's Street, Boston, Massachusetts 02215, USA*
[2] *Politecnico di Torino, Corso Duca degli Abruzzi 24, Torino 10129, Italy*
[3] *Material Science Division, Boston University, 8 Saint Mary's Street, Boston, Massachusetts 02215, USA*

(Received 12 February 2024; revised 10 April 2024; accepted 15 April 2024; published 22 May 2024)

We have investigated the carrier-transport properties of diamond using a first-principles approach. We have employed a full-band Monte Carlo model based on an electronic structure obtained from density-functional theory (DFT) augmented with Heyd-Scuseria-Ernzerhof (HSE) hybrid functionals. We have computed the carrier-phonon interaction directly employing the DFT electronic structure and phonon dispersion. Effective acoustic and optical scattering models have been calibrated against the *ab initio* results to obtain a computationally efficient transport model that retains the accuracy of the first-principles approach. Using the DFT-derived full-band structure and the calculated carrier-phonon scattering rates, we have evaluated the field-dependent drift velocities and impact-ionization coefficients and compared them to the available experimental data. We have also analyzed the temperature dependence of the carrier drift velocity up to 500 K and developed analytical models that can be used to perform device simulation based on the drift-diffusion method.

DOI: 10.1103/PhysRevApplied.21.054043

## I. INTRODUCTION

Due to its unique characteristics, diamond is a desirable material for a number of applications, ranging from high-voltage and high-power switches [1] to microwave amplifiers [2] and heat-management systems [3,4]. In fact, power electronic devices [5] are the ideal candidates to exploit the high-breakdown electric field and carrier velocities that diamond can potentially offer. Furthermore, its low susceptibility to radiation damage and high thermal conductivity make diamond the ideal material for semiconductor devices operating in harsh environments. Due to these promising qualities, diamond has been the focus of a protracted research effort spanning several decades.

While the advantages that diamond provides are widely recognized, challenges with material growth, processing, and doping have hampered the adoption of diamond as a conventional microelectronics material. Nevertheless, progress is being made in the development of both high-power diodes [6,7] and switching devices [8,9], and transistors for radio-frequency and microwave applications [2,10]. Different approaches have been developed to engineer $p$- and $n$-type layers, including substitutional incorporation, ion implantation, and transfer doping [5]. Due to the high activation energies and the resulting limited activation efficiency, very large doping levels on the order of $10^{20}$ cm$^{-3}$ are invariably required to obtain modest carrier concentration levels. As a result, the carrier-transport properties are often modified from band transport to variable-range hopping conduction. Consequently, reliable measurement of the true material transport properties is difficult and limited to intrinsic layers [11–13] or natural diamond samples [14,15].

One promising application of diamond includes lateral devices both for microwave and switching applications, which have been implemented using surface treatments that induce two-dimensional hole gas (2DHG) [16]. Unfortunately, electrical stability over time of this kind of device is difficult to achieve, which necessitates alternative methods for creating a 2DHG, such as the deposition of an acceptor layer. Nevertheless, the long-term reliability of these devices is still not well understood. As a result, to fully exploit the properties of diamond, it is likely that modulation doping using heterostructures will need to be developed. A possible candidate for realizing such a goal is cubic boron nitride ($c$-BN), which is predicted [17] to have transport properties similar to those of diamond. Since the valence-band offset between $c$-BN and diamond is predicted to be approximately 1.86 eV, a delta-doped $c$-BN barrier layer on diamond could potentially yield a 2DHG.

In this work, we perform first-principles calculations of the fundamental carrier-transport properties in diamond using the Monte Carlo method. Calculations of carrier velocities and energies are performed along the ⟨100⟩, ⟨110⟩, and ⟨111⟩ crystallographic directions for electric

*Corresponding author: bellotti@bu.edu

 © 2024 American Physical Society

fields up to 10 MV cm$^{-1}$ and variable temperature. We also present parametric models for the temperature- and field-dependent velocities, which are crucial for accurate device modeling, with the parametrization provided in Sec. A. In addition, impact-ionization coefficients are calculated up to 50 MV cm$^{-1}$ and the breakdown fields of diamond are computed.

The paper is organized as follows. In Sec. II, we describe the density-functional-theory (DFT) model used for the electronic structure and the lattice dynamics of diamond. In Sec. III, we outline the first-principles approach used to compute the carrier-phonon scattering rates. In Sec. IV, we present the calculated transport properties and, finally, in Sec. V we summarize the findings.

## II. ELECTRONIC STRUCTURE AND LATTICE DYNAMICS

Carrier-transport studies performed within the framework of the full-band Monte Carlo (FBMC) simulation approach have traditionally relied on an electronic structure description based on the empirical pseudopotential method (EPM). The quality of the EPM electronic structure depends on the availability of reliable experimental data to determine the screened periodic atomic potential, which is subsequently used in the crystal Hamiltonian. For materials that are technologically immature, it is very difficult to collect sufficient experimental information to generate an accurate electronic structure using EPM. In the case of diamond, Watanabe and coworkers [18] have used a transport model based on an EPM band structure. Subsequently, Kamakura and coworkers [19] have pointed out that calculations based on the EPM cannot reproduce some experimental breakdown-voltage data. This issue has been traced back to specific features of the EPM electronic structure at high electron energies. To avoid such issues, we have employed an *ab initio*–computed electronic structure and carrier-phonon scattering rates in the FBMC simulations.

The electronic structure of diamond has been obtained using the QUANTUM ESPRESSO (QE) package [20,21]. The SG15 optimized norm-conserving Vanderbilt (ONCV) pseudopotential [22,23] has been used to express the core-valence interactions. The Heyd-Scuseria-Ernzerhof (HSE) hybrid functional [24,25] with 28% of exact exchange gives a 5.48-eV indirect energy gap, which is close to the experimentally obtained value of 5.50 eV [26]. The DFT-HSE method has been chosen to calculate the band structure over other methods, such as the GW formalism, for its combination of accuracy and computational efficiency. While the GW formalism has the potential to be more accurate than the DFT-HSE approach used in this work, it is also dependent on the type of approximation used. Kamakura and coworkers [19] have relied on quasiparticle self-consistent GW (QSGW), which is known to overestimate band gaps in solids. The band gap of diamond predicted by QSGW is 6.43 eV, well above the experimental value of 5.50 eV [27]. Inclusion of vertex correction would overcome this problem but it is often computationally prohibitive. On the other hand, HSE is computationally less expensive and the experimental gap value can be obtained by adjusting a single parameter (the amount of exact exchange, 28% in our calculations).

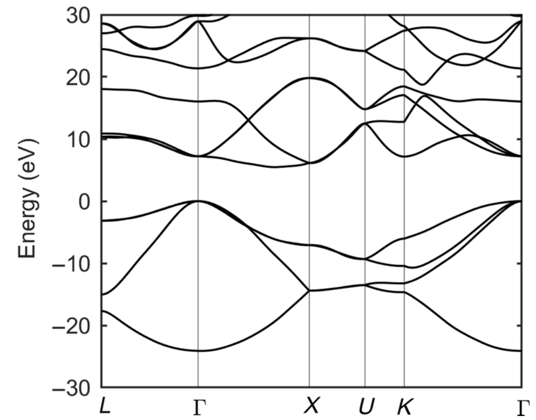


FIG. 1. The electronic structure of diamond computed using the DFT-HSE approach.

The FBMC simulations require a database of the energies and wave functions sampled across the irreducible wedge (IW) of the first Brillouin zone (FBZ). The wave functions used in this work are expanded in plane waves with a kinetic energy cutoff of 80 Ry. The calculated electronic structure for diamond is presented in Fig. 1. The volume of the IW is divided into cubic elements, with energies and wave functions evaluated at each corner and once at each edge of the cube. Within each cube, the energies and velocities of the carriers are interpolated using serendipity interpolation functions [28]. Additional mesh refinements are placed at or near valley minima to improve the accuracy of interpolation at low to moderate electric fields [29]. For diamond, these refinements are placed around Γ and along the Γ-$X$ axis to account for the valence-band maxima and the conduction-band minima, respectively. Each refined cubic element is subdivided into 216 smaller cubic elements with the same placement of $\boldsymbol{k}$ points at the corners and edges. In total, 130 331 $\boldsymbol{k}$ points are used in the sample over the entire IW, with energies and wave functions computed at each $\boldsymbol{k}$ point.

## III. CARRIER-PHONON INTERACTION

Another important quantity needed to develop a transport model for diamond is the phonon dispersion, which is necessary to evaluate the carrier-phonon scattering rates. The phonon dispersion is obtained within density-functional perturbation theory (DFPT) [30,31], implemented in the QE package with an $8 \times 8 \times 8$ grid of phonon

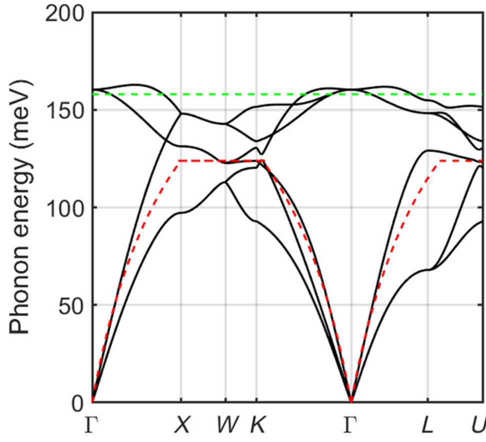


FIG. 2. The calculated phonon dispersion in diamond. The solid black lines represent the phonon energies computed using DFT. The dashed red and green lines represent the effective acoustic and optical phonon dispersions, respectively.

**q** vectors using Perdew-Burke-Ernzerhof (PBE) functionals [32]. In Fig. 2, we present the calculated phonon dispersion for diamond. For this calculation, the use of a hybrid functional is not critical and the PBE model significantly reduces the computing time.

Using the *ab initio*–computed phonon dispersion, along with the DFT-HSE electronic structure, the carrier-phonon scattering rates can be also evaluated using an *ab initio* approach. The contribution to the total scattering rate from each phonon branch is evaluated by computing the matrix elements that are derived from the self-consistent calculation of the crystal potential.

The EPW code [33], which implements the aforementioned approach, is employed for this work and the contributions (emission plus absorption) of each phonon branch (three acoustic and three optical) are stored separately. The electron-phonon coupling on fine sampling ($60 \times 60 \times 60$ for both **k** and **q** vectors) on the BZ is computed through maximally localized Wannier functions (MLWFs) [34] and generalized Fourier interpolation [35]. Convergence of the scattering rates is checked by using progressively finer **k** and **q** grids.

The DFT-HSE–computed energy eigenvalues and wave functions are also used to compute the carrier-phonon scattering rates using a simplified phonon-dispersion model for use in the FBMC simulations. In these calculations, a single *effective acoustic* mode and a single *effective optical* mode have been used to fully describe the dispersion, shown in Fig. 2. The use of the *effective* scattering modes within the FBMC transport models gives information on the final $\boldsymbol{k}$ state after scattering, in addition to simplifying the treatment of the scattering processes and significantly reducing the execution time.

The rates computed using the simplified models are then scaled to match the rates computed by EPW using a set of deformation potentials, $D_{\text{ac}}(E)$ and $D_tK(E)$, for the acoustic and optical scattering rates, respectively. The acoustic $D_{\text{ac}}(E)$ *effective* deformation potential has been determined by comparing the total scattering rates obtained using the *effective* phonon modes, with the sum of the three acoustic scattering rates computed using EPW. The same procedure is applied to determine the optical $D_tK(E)$ *effective* deformation potential, using the sum of the three optical *ab initio* scattering rates. Additional information about the use of the effective scattering models can be found in Ref. [17], where the same approach has been used for the study of carrier-transport properties of *c*-BN. The rates incorporated into FBMC are computed using the following equations originally derived from Fermi's golden rule for the acoustic (ac) [36] and optical (op) [36] absorption and emission processes and requires integrating for each initial point, $\boldsymbol{k}$, in each initial band, $n$, to each final point, $\boldsymbol{k}'$, in each final band, $n'$:

$$\frac{1}{\tau_{\text{ac}}^{\pm}(n,\boldsymbol{k})} = \frac{2\pi}{\hbar}\sum_{n'}\int_V d\boldsymbol{k}' \frac{|\boldsymbol{q}|\pi(D_{\text{ac}}(E))^2}{V\rho\omega_{\text{ac}}}\left\{N_q + \frac{1}{2} \pm \frac{1}{2}\right\} \times |I(n,\boldsymbol{k},n',\boldsymbol{k}')|^2 \times \delta[E(\boldsymbol{k}') - E(\boldsymbol{k}) \mp \hbar\omega_{\text{ac}}(\boldsymbol{q})], \tag{1}$$

$$\frac{1}{\tau_{\text{op}}^{\pm}(n,\boldsymbol{k})} = \frac{2\pi}{\hbar}\sum_{n'}\int_V d\boldsymbol{k}' \frac{\pi(D_tK(E))^2}{V\rho\omega_{\text{op}}}\left\{N_q + \frac{1}{2} \pm \frac{1}{2}\right\} \times |I(n,\boldsymbol{k},n',\boldsymbol{k}')|^2 \times \delta[E(\boldsymbol{k}') - E(\boldsymbol{k}) \mp \hbar\omega_{\text{op}}(\boldsymbol{q})]. \tag{2}$$

In these equations, $e$ is the electronic charge, $\boldsymbol{q}$ is the phonon wave vector, $N_q$ is the phonon number, $\omega$ and $\hbar\omega$ are the phonon angular frequency and phonon energy, $\rho$ is the density of diamond, and $I(n,\mathbf{k},n',\mathbf{k}')$ is the overlap integral between the corresponding Bloch wave functions. For momentum conservation, the condition $\boldsymbol{k}' = T_{\text{FBZ}}(\boldsymbol{k}+\boldsymbol{q})$ needs to be satisfied, where $T_{\text{FBZ}}(\boldsymbol{k}+\boldsymbol{q})$ stands for the transformation of the $k$ vector, $\boldsymbol{k}+\boldsymbol{q}$, into the FBZ. The term $D_{\text{ac}}(E)$ is the energy-dependent acoustic phonon deformation potential and $D_tK(E)$ is the energy-dependent optical phonon deformation potential. In these equations, $N_q + \frac{1}{2} + \frac{1}{2}$ is used for emission processes and $N_q + \frac{1}{2} - \frac{1}{2}$ is used for absorption processes. The Umklapp scattering processes are also included in the calculations.

The process of matching the two sets of scatterings (*ab initio* and *effective*) reveals that the widely used assumption that $D_{\text{ac}}$ and $D_tK$ can be treated as constant fitting parameters is not valid and that both $D_{\text{ac}}(E)$ and $D_tK(E)$ should be treated as energy-dependent quantities, obtained matching the effective with the *ab initio* scattering rates for each mechanism. In Fig. 3, we present the total electron-phonon acoustic scattering rate computed using the full phonon dispersion from DFT-PBE (solid black line) with DFT-HSE wave functions and a single acoustic *effective*

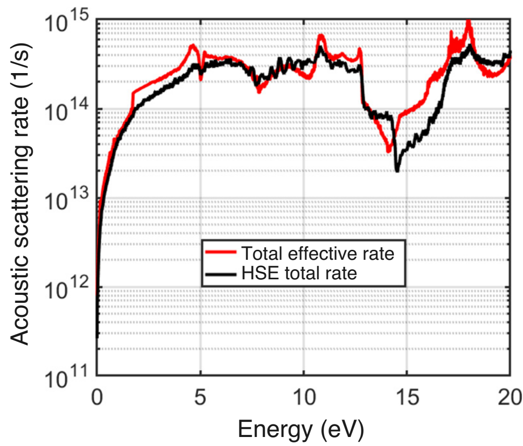


FIG. 3. A comparison between the total electron acoustic scattering rate computed using the full phonon dispersion from DFT HSE (solid black line) and a single acoustic effective phonon mode (solid red line).

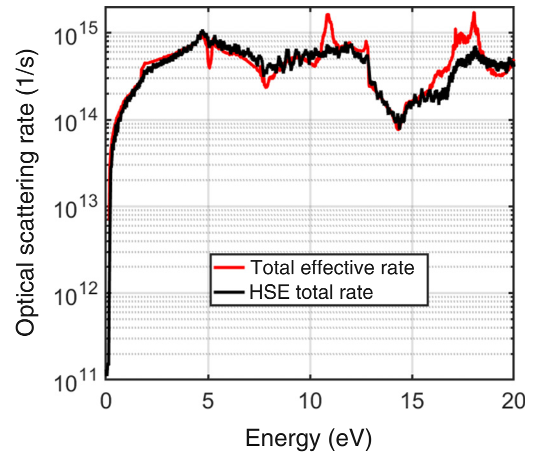


FIG. 5. A comparison between the total electron optical scattering rate computed using the full phonon dispersion and electronic structure from DFT HSE (solid black line) and a single optical effective phonon mode (solid red line).

phonon mode (red solid line) with energy-dependent values of $D_{\rm ac}$. In the same way, in Fig. 4, we present the same quantities for the case of the hole-phonon acoustic scattering rate computed using the full phonon dispersion from DFT-PBE (solid black line) and DFT-HSE wave functions and a single acoustic effective phonon mode (solid red line) with energy-dependent values of $D_{\rm ac}(E)$

The same procedure has been applied to obtain the *effective* scattering rates for optical phonons. In Fig. 5, we present the comparison between the total electron-phonon optical scattering rate computed using the full phonon dispersion from DFT PBE with DFT-HSE wave functions (solid black line) and a single optical phonon *effective* mode (solid red line). Finally, in Fig. 6, we show the comparison between the total hole optical scattering rate computed using the *ab initio* model (solid black line) and a single *effective* optical phonon mode (solid red line).

The last scattering mechanism considered in the FBMC simulations is the impact-ionization transition rate. This quantity provides the energy-dependent rate at which an electron or hole will ionize an electron from the valence band into the conduction band, creating an electron-hole pair. In this process, the initiating carrier will lose energy equal to the band gap. The impact-ionization scattering rates are computed to the first order using previously derived methods based on Fermi's golden rule [37–41]. In Figs. 7 and 8, we present the calculated electron and hole impact-ionization scattering rates, respectively. In both

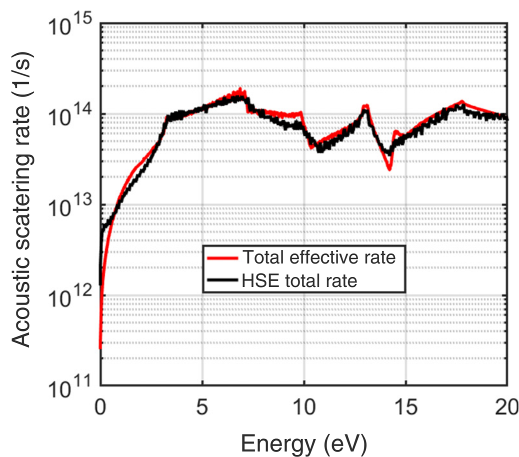


FIG. 4. A comparison between the total hole acoustic scattering rate computed using the full phonon dispersion from DFT HSE (solid black line) and a single acoustic effective phonon mode (solid red line).

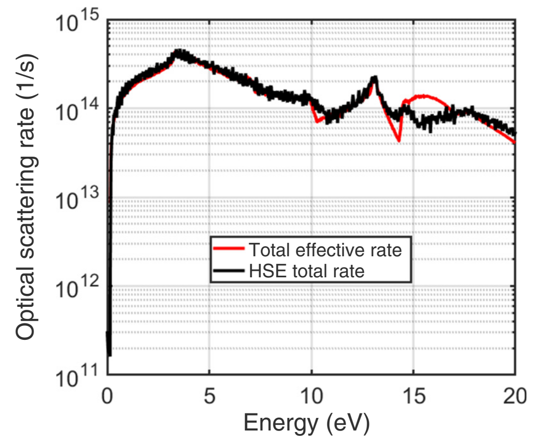


FIG. 6. A comparison between the total hole optical scattering rate computed using the full phonon dispersion and electronic structure from DFT HSE (solid black line) and a single effective optical phonon mode (solid red line).

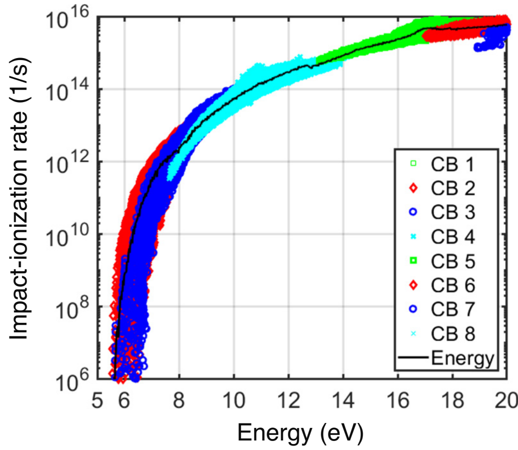


FIG. 7. The calculated electron impact-ionization scattering rate. The open symbols are the *k*-dependent values and the solid black line is the energy-averaged scattering rate.

figures, the symbols represent the values of the rates computed for a given ***k*** point in the IW and band (conduction or valence) and the solid black line is the corresponding energy-dependent rate used in the FBMC simulations.

All the scattering rates presented in this section are computed on a grid of 130 331 ***k*** points in the irreducible wedge of the first Brillouin zone and subsequently averaged over the energy scale. In this work, we do not consider the effect of scattering due to ionized impurities. Consequently, we assume that the results presented in the following sections should be considered applicable to natural diamond with a very low impurity concentration, as found in Refs. [11,13–15]

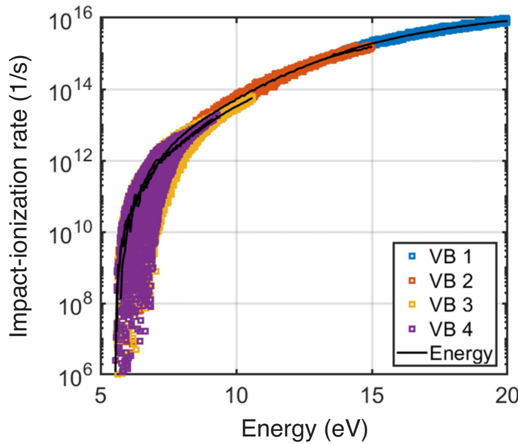


FIG. 8. The calculated hole impact-ionization scattering rate. The open symbols are the *k*-dependent values and the solid black line is the energy-averaged scattering rate.

## IV. TRANSPORT PROPERTIES

We have computed the transport properties of undoped or natural diamond using the full electronic structure presented in Sec. II and the scattering rates presented in Sec. III, within a full-band Monte Carlo (FBMC) simulator [42]. A particle ensemble composed of 2500 electrons and 2500 holes is used to obtain statistics on the carrier velocities and energies for electric field strengths ranging from 500 V $\mathrm{cm}^{-1}$ to 10 MV $\mathrm{cm}^{-1}$. Furthermore, we have also evaluated the impact-ionization coefficients for both carrier species up to a field of 50 MV $\mathrm{cm}^{-1}$.

### A. Carrier drift velocities at 300 K

Several groups have measured the electron [11,14,43] and hole [11,15,43] drift velocities in diamond. The experimental data are limited to electric field strengths below 100 KV/cm [14,15] and in the linear transport regime below 1 kV/cm [11,43]. Furthermore, temperature-dependent measurements are also available up to 700 K.

In Fig. 9, we present a comparison between the measured and computed electron drift velocity in diamond as a function of the applied electric field strength at 300 K. The red square, green diamond, and blue circles are the experimental values from Ref. [14]. The solid blue, dashed red, and dash-dot green lines represent the values calculated in this work for electric fields applied in the ⟨100⟩, ⟨110⟩, and ⟨111⟩ directions. The calculated values are in good agreement with the experimental data without the use of additional deformation potentials besides the ones used to match the *ab initio* scattering rates. The values of the initial mobility computed from the calculated velocity are approximately 2400 $\mathrm{cm}^2$ $\mathrm{V}^{-1}$ $\mathrm{s}^{-1}$, in agreement with other calculated [44] and measured [11,12,14,43] values. Above 1 kV $\mathrm{cm}^{-1}$, anisotropy can be observed in the drift velocities along different crystallographic directions, with the velocity in the ⟨110⟩ direction higher than along the ⟨100⟩ direction. This behavior is similar to that of silicon and can be found in other semiconductors with a many-valley band structure with ellipsoidal conduction-band minima along the ⟨100⟩ equivalent directions.

In Fig. 10, we present the hole field-dependent drift velocity at 300 K. The red squares, blue circles, and black triangles are the experimental values from Refs. [11,15]. The solid blue, dashed red, and dash-dot green lines represent the values calculated in this work for electric fields applied along the ⟨100⟩, ⟨111⟩, and ⟨110⟩ directions. For holes, the experimental data and calculated values show good agreement. The estimated values of the hole mobility are approximately 2340 $\mathrm{cm}^2$ $\mathrm{V}^{-1}$ $\mathrm{s}^{-1}$ in the ⟨100⟩ direction and approximately 1830 $\mathrm{cm}^2$ $\mathrm{V}^{-1}$ $\mathrm{s}^{-1}$ in the ⟨110⟩ direction. These mobility values show a reasonable agreement with other calculated [44] and measured [11,12,14,43] values. It is interesting to note that, at least for natural or undoped diamond, the drift velocities for both carrier

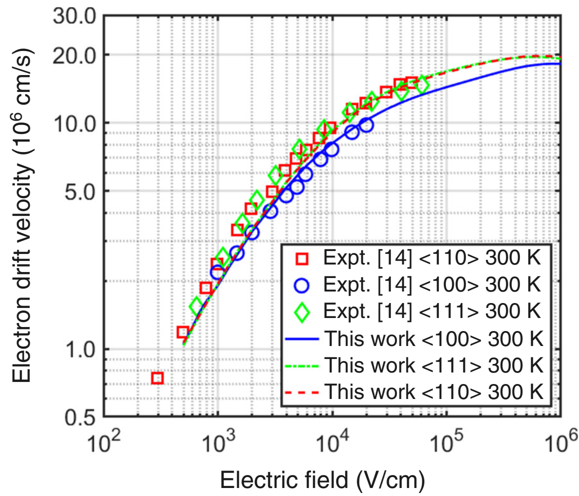


FIG. 9. The measured and computed electron drift velocity in diamond as a function of the applied electric field strength. The red square, green diamond, and blue circles are the experimental values from Ref. [14]. The solid blue, dashed red, and dash-dot green lines are the values calculated in this work.

species are very similar. It should be noted that diamond films with high defect densities, and/or those that are doped to a level where hopping transport is induced, are expected to have much lower carrier mobilities [45,46].

### B. Temperature-dependent drift velocities

Due to the potential applications of diamond as a material for operation at high temperature, it is important to estimate the transport coefficients for temperatures above 300 K. It is important to reiterate that the calculated velocities of this work are the direct results of the electronic structure and scattering rates evaluated from first principles. The results are compared to temperature-dependent drift velocity data measured along the ⟨110⟩ [14,47] and ⟨100⟩ [11,14,15,43] crystallographic directions. For the most accurate calculations of temperature-dependent drift velocities, the scattering rate and energy structure should be changed for FBMC simulations at each temperature. In this work, we show that recomputing the carrier-phonon scattering rates without altering the energy structure for each temperature yields satisfactory results for temperatures of 400 K and 500 K.

In Fig. 11, we present a comparison between the measured and calculated temperature-dependent electron and hole drift velocities along the ⟨100⟩ and ⟨110⟩ crystallographic directions. For electrons in the ⟨100⟩ direction, good agreement between the calculated and measured values from Ref. [11] is observed for temperatures of 300 K and 400 K. The measured values at 460 K are just above the calculated values at 500 K. In the ⟨110⟩ direction, good agreement between the calculated and measured values is attained only at 300 K; however, for higher temperatures, the model underestimates the electron velocity.

The same analysis has been performed for holes and the drift velocity has been evaluated for electric fields applied along the ⟨110⟩ and ⟨100⟩ directions. For holes, the calculated values are in good agreement with the experiment for all temperatures. In Sec. A 1, we provide a parametric representation of the temperature and field-dependent velocity as a function of a limited set of parameters that are provided for each crystallographic direction.

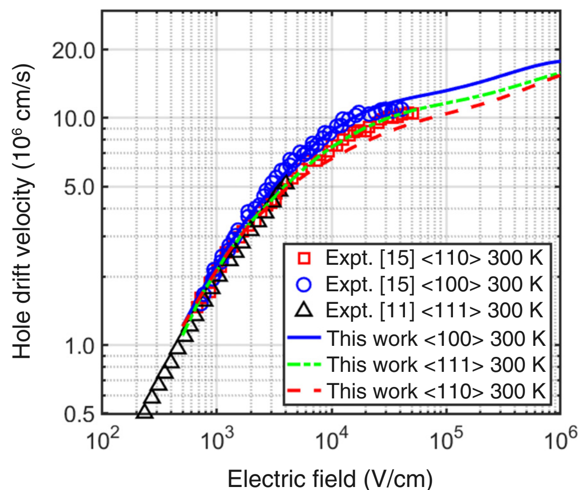


FIG. 10. The red square, and blue circles are the experimental values from Ref. [15]. The black triangles are experimental values from Ref. [11]. The solid blue, dashed red, and dash-dot green lines are the values calculated in this work.

### C. Impact-ionization coefficients

The second set of transport parameters of interest is the ionization coefficients. The operational limit of diamond-based power devices is determined by the breakdown characteristics. While the specific device design may ultimately prevent us from reaching the intrinsic limit of the material, knowledge of the ionization coefficients permits us to establish a benchmark for the ultimate material and device performance. The impact-ionization coefficients are defined as the inverse of the mean free path between two impact-ionization events.

In Fig. 12, we present the impact-ionization coefficients data available in the literature. Both experimental [48–51] and theoretical [19,53] data are presented. The experimental data in Figs. 12(a) and 12(b) have been extracted from Schottky-barrier-diode breakdown data [48–51], the values in the data set of Fig. 12(d) [52] have been inferred by scaling the data for silicon and silicon carbide using the difference in energy gap. The theoretical data in Fig. 12(c) [53] and Fig. 12(e) [19] have been obtained from full-band Monte Carlo models that include empirical

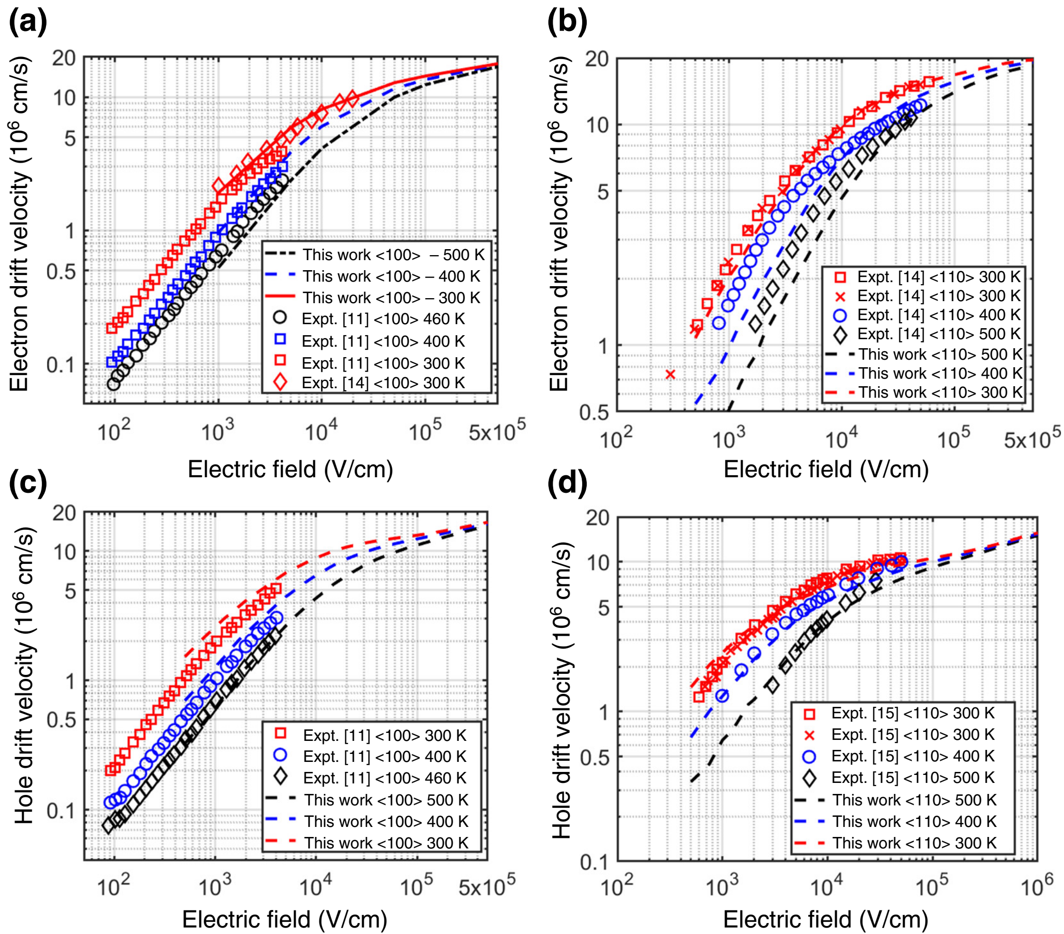


FIG. 11. The measured and computed electron (top row) and hole (bottom row) drift velocity in the ⟨100⟩ (left column) and ⟨110⟩ (right column) crystallographic directions in diamond as a function of the applied electric field. The values obtained in this work are plotted with dashed lines and experimental values are plotted with symbols. The experimental values are from Refs. [11,14,15].

pseudopotential and *ab initio* models, respectively. The available ionization coefficients show a large spread in values for both electrons and holes.

In this work, the impact-ionization coefficients are computed for fields ranging from 2 MV $\mathrm{cm}^{-1}$ to 50 MV $\mathrm{cm}^{-1}$, with the ionization coefficients evaluated as the average distance between ionizations. The calculated electron and hole impact-ionization coefficients in diamond as a function of the inverse applied electric field strength along the ⟨111⟩, ⟨100⟩, and ⟨110⟩ directions are presented in Fig. 13. The hole and electron coefficients are represented by the red and blue lines and markers, respectively. For low ionization coefficients below $10^3$ $\mathrm{cm}^{-1}$, the low number of ionizations may create some uncertainty in the results. For example, the confidence interval of the hole ionization coefficient at 2 MV $\mathrm{cm}^{-1}$ is less than 100 $\mathrm{cm}^{-1}$, leading to a significant uncertainty in the calculated values of approximately 7% for a 99% confidence level. However, a much higher hole ionization coefficient of $8\times10^3$ $\mathrm{cm}^{-1}$ for a field of 3 MV $\mathrm{cm}^{-1}$ results in an uncertainty of less than 1% for a 99% confidence level.

It should be noted that the calculated values of this work are similar to those obtained by Kamakura and coworkers [19], which are presented in Fig. 12. They have used a model similar to ours but based on DFT within the GW framework. We can observe that our calculated values are generally slightly higher than the ones from Ref. [19] but present a similar qualitative trend as a function of the inverse electric field. This is not unexpected, since the two models are based on similar *ab initio* approaches. We can also note that both models suggest that there is very little anisotropy for electric fields applied in different crystallographic directions. Additionally, we observe that the ionization coefficient values for electrons are significantly lower than those for holes. Another feature of the calculated ionization coefficients is the dual-slope behavior, where at higher field strengths, the values of the coefficients increase more rapidly. This indicates that at lower fields, the dependence of the ionization coefficients can be explained by Shockley's lucky-electron theory, whereas for fields above 10 MV $\mathrm{cm}^{-1}$ in magnitude, the ionization coefficients seem to follow Wolff's theory [54]. At

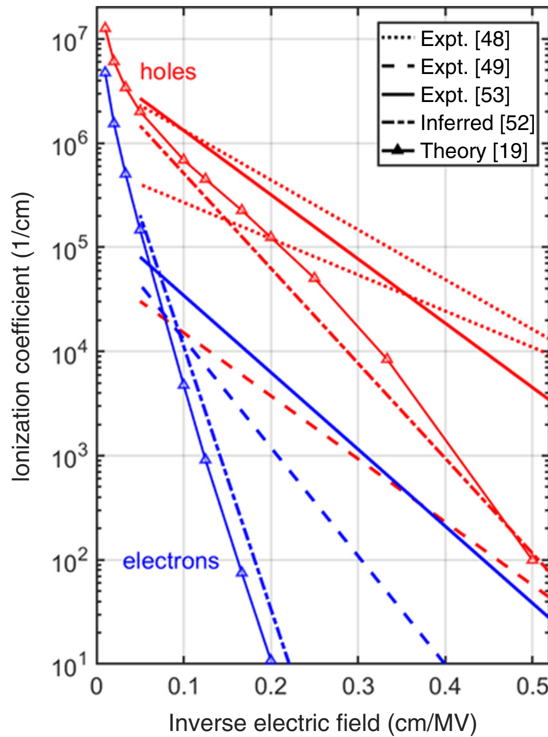


FIG. 12. The theoretical and experimental impact-ionization coefficient data available in the literature. The experimental data have been extracted from Schottky-barrier-diode breakdown data [48–51], while the values in data set [52] have been inferred by scaling the data for silicon and silicon-carbide using the difference in the energy gap. The theoretical data [53] and [19] have been obtained from full-band Monte Carlo models that include an empirical pseudopotential and *ab initio* models.

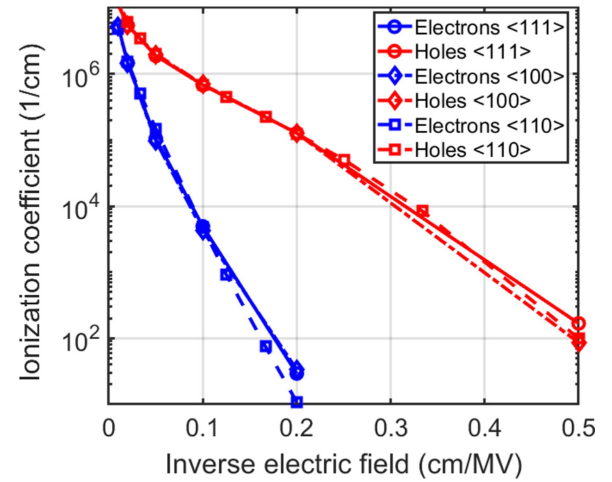


FIG. 13. The calculated electron and hole impact-ionization coefficients in diamond as a function of the inverse applied electric field strength at 300 K. The solid red line with circles, the dot-dash red line with diamonds, and the dashed red line with squares are the calculated values for holes when the electric fields are applied in the ⟨111⟩, ⟨100⟩, and ⟨110⟩ directions, respectively. The solid blue line with circles, the dot-dash blue line with diamonds, and the dashed blue line with squares are the calculated values for electrons when the electric fields are applied in the ⟨111⟩, ⟨100⟩, and ⟨110⟩ directions, respectively.

10 MV cm$^{-1}$, the value of the electron ionization coefficient is 2 orders of magnitude lower than the one for holes. This indicates that even at high electric field strengths, the impact-ionization process is dominated by holes rather than electrons. Furthermore, the large difference between the coefficients points to a soft breakdown process.

The experimental validation of the calculated values requires the direct or indirect measurement of the impact-ionization coefficients. The extraction of the impact-ionization coefficients from device data is a difficult process for any semiconductor material. For diamond, this is particularly challenging due to many factors. First, it is difficult to fabricate devices with high enough quality to observe true avalanche-breakdown behavior. The high concentration of donor and acceptors needed to obtain modest carrier concentration (e.g., boron) may lead to defect impact ionization that could mask the onset of band-to-band multiplication process [55,56]. Second, the device geometry and the presence of a complex electric field profile make a simplified one-dimensional (1D) model unsuitable for coefficient extraction. Finally, the quality of contacts and fringe fields in Schottky diodes further complicates the extraction procedure. Hiraiwa and coworkers [48,49] and Driche and coworkers [51] have extensively analyzed and computed the breakdown voltage of Schottky barrier and *p*-*n* junction diodes using a 2D drift-diffusion numerical simulation model. They have found that in the case of Schottky barrier diodes, the available ionization coefficient values lead to an overestimation of the breakdown voltage, approximately by a factor of 2 when using Kamakura [19] coefficients.

From these results, it is clear that further work is needed to measure ionization coefficients with appropriate test structures that minimize fabrication issues.

### D. Breakdown characteristics

To benchmark our calculated ionization coefficients against experimental data and other theoretical models, we have analyzed the breakdown voltage and the related maximum electric field of unilateral *p*-*n* junctions. We have determined the breakdown characteristics of the junction using two approaches. First, we have performed a direct simulation of the multiplication gain using a Monte Carlo model. This approach does not require the use of the ionization coefficients, since the breakdown process is simulated directly, tracking the offspring results from the impact-ionization process. Alternatively, we have evaluated the breakdown voltage by solving the ionization

integral [57,58], using the ionization coefficients derived in this work and other values presented in Refs. [48,49,51].

The breakdown field is computed using our FBMC simulator for a 1D $p^-$-$n^+$ diode. The donor density in the $n^+$ is maintained fixed at $10^{20}$ cm$^{-3}$, while the acceptor doping density of the $p^-$ varies from $10^{15}$ cm$^{-3}$ to $10^{19}$ cm$^{-3}$. We assume that the dopants are fully ionized. While for diamond this is a crude approximation, this provides a way of comparing different results on an equal footing.

Although simulations of *pn* diodes would typically require the incorporation of impurity scattering models due to the high concentration of dopants, we have chosen to not include them in the calculations of breakdown. This is because at the high fields where impact ionization and breakdown occur, optical and acoustic deformation potential scatterings are the dominant mechanisms and ionized impurity scattering is not effective in relaxing the carrier momentum as a result of the small scattering angles.

The breakdown calculations have been performed by computing the average hole multiplication gain when carriers are injected at the $p^-$-$n^+$. Subsequently, we have evaluated the values of the maximum electric field extrapolating the gain values. Specifically, we have defined the breakdown field as the electric field strength for which the gain is $10^6$. The normalized critical electric field for the material can be extracted using the approach in Ref. [57].

As the applied voltage approaches the breakdown value, the gain increases superexponentially. This can result in a free carrier density that effectively screens the electric field reducing the multiplication gain [64]. The approach used in this work to evaluate the breakdown voltage assumes that the number of injected carriers is small and that even for a nominal gain of $10^6$, the screening effect is not the limiting factor.

The values of the maximum electric field at breakdown calculated using our model are shown in Fig. 14 and are compared to breakdown fields computed theoretically using *ab initio* models [19], experimentally determined [60–63], and obtained by fitting the ionization coefficients to experimental breakdown voltages [48,49].

We can note that the peak electric field strength calculated using the ionization integral approach and from a direct evaluation through FBMC is similar to what has been theoretically obtained by Kamakura and coworkers [19]. Furthermore, the calculated results are in reasonable agreement with the experimentally derived values from Refs. [60–62]. However, the reported breakdown field of 20 MV cm$^{-1}$ for a doping density of $10^{18}$ cm$^{-3}$ [63] is still much higher than the *ab initio* predicted values, even though the values obtained from a direct FBMC calculation are closer to the experimental result. It is not clear why such a large discrepancy is present for this particular experimental value. It is also important to point out that the results from Refs. [48,49] have been obtained using an ionization coefficient derived fitting all the available

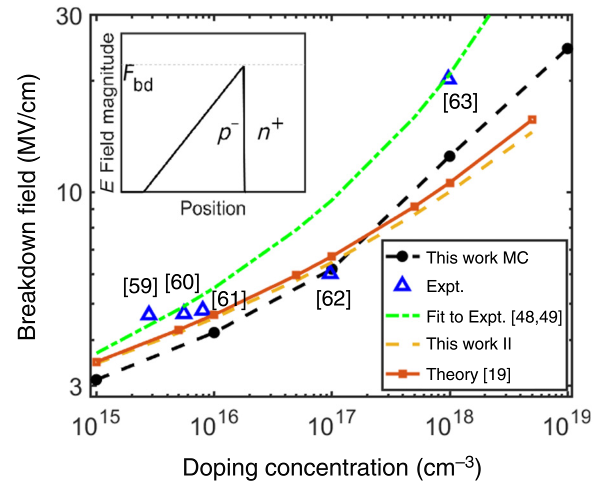


FIG. 14. The maximum electric field value at the breakdown as a function of the $p$-type doping density for a $p^-$-$n^+$ junction. The experimental values are from Refs. [59–63]. The data from Ref. [61] estimate their doping to be $<8 \times 10^{15}$ cm$^{-3}$ but the data point is placed at $8 \times 10^{15}$ cm$^{-3}$. The data in Refs. [48,49] are obtained using ionization-coefficient values fitted to the experimental values. The values in Ref. [19] have been computed using ionization coefficients obtained from a theoretical model based on DFT GW. The dashed black line with circles represent the values calculated in this work by a direct simulation of the multiplication gain. The dashed yellow line with circles represents the values calculated by solving the ionization integral and using the ionization coefficients derived from the FBMC model. The inset of the figure shows the typical field profile of the junction, with the breakdown field, $F_{bd}$, defined as the peak field.

experimental data. As a result, this particular data set can also reproduce the maximum field reported in Ref. [63].

The difference between the peak field values obtained using the direct simulation (dashed black line with circle) and the solution of the ionization integral (dashed yellow line with circle) is likely the result of the analytical model [65] used to fit the calculated ionization coefficients presented in Fig. 13, which cannot reproduce the change of slope at the lowest and highest values of the inverse electric field. Furthermore, at high doping densities, above $5 \times 10^{17}$ cm$^{-3}$, the depletion regions become relatively short, less than 1 $\mu$m. In this case, the assumption that the ionization coefficients are a local function of the electric field [65] may no longer be valid.

## V. CONCLUSIONS

We have presented a model of the carrier-transport parameters in undoped diamond obtained using a first-principles approach. We have computed the electronic structure of diamond using a density-functional approach that includes hybrid functionals (DFT HSE). Subsequently, we have computed the carrier-phonon scattering rates

directly from first principles and we have extracted the acoustic and optical deformation potentials. Finally, using a full-band Monte Carlo model, we have computed the carrier drift velocities as a function of the lattice temperature and electric field, as well as its ionization coefficients.

We find that the fitting parameter free *ab initio* model can reproduce the measured values of both electron and hole drift velocities as a function of the electric field magnitude and temperature and along different crystallographic directions. The calculated values are in good agreement with those measured by several groups for natural diamond. We have also developed analytical models of the field- and temperature-dependent carrier velocities to be used in conjunction with numerical device simulators based on the drift-diffusion method.

To date, there are no direct experimental measurements of the impact-ionization coefficients in diamond. Several groups have inferred their values by fitting analytical models to breakdown-voltage values measured for a few device structures. As a result, we have compared the impact-ionization-coefficient values obtained in this work both with other theoretical predictions and with values inferred from measured breakdown voltages. Furthermore, we have also used our transport model and ionization coefficients to compute the breakdown voltages and peak electric fields of a unilateral $p^-$-$n^+$ junction.

We find that our ionization coefficients exhibit the same dependence on the electric field of the ionization coefficients as predicted by Kamakura and coworkers [19]. However, we obtain slightly higher coefficients for holes and lower values for electrons. Moreover, the calculated value of the peak electric field at breakdown in a unilateral $p^-$-$n^+$ junction as a function of the $p$-doping level is in reasonable agreement with the values from other models and experimental data below the doping level of $5 \times 10^{17}$ cm$^{-3}$.

While the work presented in this paper provides a contribution to understanding the carrier transport in diamond, additional work is needed. From the experimental standpoint, we believe that a concerted effort is needed to develop a device structure that will enable the direct measurement of ionization coefficients as a function of temperature. Moreover, from the theoretical point of view, we think that a quantitative model to describe defect-assisted impact-ionization needs to be developed to assess the relative contribution of this process to the carrier multiplication phenomena.

## ACKNOWLEDGMENTS

This work was supported by the U.S. Army Research Office RF-Center, managed by Dr. T. Oder (Grant No. #W911NF-22-2-0158), and by the U.S. Army Research Laboratory through the Center for Semiconductor Modeling (Grant No. #W911NF-18-2-0027), managed by Dr. M. Reed and Dr. J. Schuster. The computational resources were provided by the Department of Defense (DoD) High Performance Computing (HPC) Systems, the 2019 Army Research Office (ARO) Defense University Research Instrumentation Program (DURIP) Award (Grant No. #W911NF-19-1-0161), and the DoD HPC Modernization program.

## APPENDIX: ADDITIONAL INFORMATION

### 1. Analytical models for the drift velocities

We have developed an analytical model to quantify the electron and hole drift velocity dependence on the electric field strength and temperature. The analytical expression that we have used to represent the drift velocity is a modified version of the Canali model [66]:

$$v_d = \frac{\mu E}{1 + \left(\frac{E}{E_R}\right)^{\alpha}} \left[1 - \beta \left(\frac{E}{E_1}\right)^{\gamma}\right],$$
$$\mu = \mu_0 \left(\frac{T}{T_0}\right)^{\eta}, \tag{A1}$$
$$E_R = E_0 \left(\frac{T}{T_0}\right)^{\delta}.$$

The parameters in Eq. (A1) are: the reference temperature $T_0 = 300$ K, the initial mobility $\mu_0$ and the mobility temperature exponent $\eta$, the reference field $E_0$ and the reference-field temperature exponent $\delta$, the saturation velocity exponent $\alpha$, the velocity reduction coefficient at high field $\beta$ and the velocity reduction exponent at very high field $\gamma$, the reference electric field strength for velocity reduction at high field $E_1$. We present the parameter values needed to reproduce the temperature-dependent electron and hole velocities in Table I.

### 2. Effective masses

We have evaluated the effective masses of electrons and holes by fitting the numerically calculated density of states (DOS) to the analytical expression of the DOS for a nonparabolic spherical band. For the DFT-HSE band, we use a

TABLE I. The fitting parameters for Eq. (A1).

| Direction | $T_0$ (K) | $\mu_0$ (cm$^2$ V$^{-1}$ s$^{-1}$) | $\eta$ | $E_0$ (V cm$^{-1}$) | $\delta$ | $E_1$ (V cm$^{-1}$) | $\gamma$ | $\alpha$ | $\beta$ |
|---|---|---|---|---|---|---|---|---|---|
| ⟨100⟩ | 300.0 | 2630.0 | −2.6 | $4.9 \times 10^3$ | 3.0 | $6.0 \times 10^6$ | 0.33 | 0.86 | 0.6 |
| ⟨110⟩ and ⟨111⟩ | 300.0 | 2650.0 | −2.6 | $6.0 \times 10^3$ | 3.0 | $6.0 \times 10^6$ | 0.33 | 0.88 | 0.6 |

TABLE II. The DOS-derived effective masses and nonparabolicity coefficients from DFT HSE.

| | Electrons | Holes | HH | LH | SO |
|---|---|---|---|---|---|
| DOS effective mass ($m_0$) HSE | 0.46 | 1.25 | 0.7 | 0.225 | 0.13 |
| Nonparabolicity coefficient (1/eV) HSE | 0.25 | 0.11 | 0.05 | 0.2 | 0.125 |

very fine energy grid in $k$ space on which we interpolate the energy values to compute the DOS. We present the DOS-derived values of the effective masses and nonparabolicity coefficients in Table II.


[1] N. Donato, N. Rouger, J. Pernot, G. Longobardi, and F. Udrea, Diamond power devices: State of the art, modelling, figures of merit and future perspective, J. Phys. D **53**, 093001 (2020).

[2] T. G. Ivanov, J. Weil, P. B. Shah, A. G. Birdwell, K. Kingkeo, and E. A. Viveiros, in *2018 IEEE/MTT-S International Microwave Symposium*, IEEE-MTT Proceedings, Vol. 2018 (Pennsylvania Convention Center, Philadelphia, Pennsylvania, 2018), p. 1461.

[3] Y. Zhou, R. Ramaneti, J. Anaya, S. Korneychuk, J. Derluyn, H. Sun, J. Pomeroy, J. Verbeeck, K. Haenen, and M. Kuball, Thermal characterization of polycrystalline diamond thin film heat spreaders grown on GaN HEMTs, Appl. Phys. Lett. **111**, 041901 (2017).

[4] K. Jagannadham, Multilayer diamond heat spreaders for electronic power devices, Solid-State Electron. **42**, 2199 (1998).

[5] S. Koizumi, H. Umezawa, J. Pernot, M. Suzuki, eds., *Power Electronics Device Applications of Diamond Semiconductors* (Woodhead Publishing, Duxford, United Kingdom, 2018).

[6] J. Butler, M. Geis, K. Krohn, J. Lawless, S. Deneault, T. Lyszczarz, D. Flechtner, and R. Wright, Exceptionally high voltage Schottky diamond diodes and low boron doping, Semicond. Sci. Technol. **18**, S67 (2003).

[7] P.-N. Volpe, P. Muret, J. Pernot, F. Omnes, T. Teraji, Y. Koide, F. Jomard, D. Planson, P. Brosselard, N. Dheilly, B. Vergne, and S. Scharnholz, Extreme dielectric strength in boron doped homoepitaxial diamond, Appl. Phys. Lett. **97**, 223501 (2010).

[8] H. Umezawa, T. Matsumoto, and S.-I. Shikata, Diamond metal-semiconductor field-effect transistor with breakdown voltage over 1.5 kV, IEEE Electron Device Lett. **35**, 1112 (2014).

[9] M. Syamsu, N. Oi, S. Okubo, T. Kageura, and H. Kawarada, Heteroepitaxial diamond field-effect transistor for high voltage applications, IEEE Electron Device Lett. **39**, 51 (2018).

[10] R. J. Trew, J.-B. Yan, and P. M. Mock, The potential of diamond and SiC electronic devices for microwave and millimeter-wave power applications, Proc. IEEE **79**, 598 (1991).

[11] M. Gabrysch, S. Majdi, D. Twitchen, and J. Isberg, Electron and hole drift velocity in chemical vapor deposition diamond, J. Appl. Phys. **109**, 063719 (2011).

[12] J. Isberg, J. Hammersberg, E. Johansson, T. Wikstrom, D. Twitchen, A. Whitehead, S. Coe, and G. Scarsbrook, High carrier mobility in single-crystal plasma-deposited diamond, Science **297**, 1670 (2002).

[13] H. Pernegger, S. Roe, P. Weilhammer, V. Eremin, H. Frais-Kölbl, E. Griesmayer, H. Kagan, S. Schnetzer, R. Stone, W. Trischuk, D. Twitchen, and A. Whitehead, Charge-carrier properties in synthetic single-crystal diamond measured with the transient-current technique, J. Appl. Phys. **97**, 073704 (2005).

[14] F. Nava, C. Canali, C. Jacoboni, L. Reggiani, and S. Zozlov, Electron effective masses and lattice scattering in natural diamond, Solid State Commun. **33**, 475 (1980).

[15] L. Reggiani, S. Bosi, C. Canali, F. Nava, and S. Kozlov, Hole-drift velocity in natural diamond, Phys. Rev. B **23**, 3050 (1981).

[16] H. Kawarada, Hydrogen-terminated diamond surfaces and interfaces, Surf. Sci. **26**, 205 (1996).

[17] M. Zhu, M. Matsubara, and E. Bellotti, Carrier transport in cubic boron nitride: First-principles and semiempirical models, Phys. Rev. Appl. **20**, 034055 (2023).

[18] T. Watanabe, T. Teraji, T. Ito, Y. Kamakura, and K. Taniguchi, Monte Carlo simulations of electron transport properties of diamond in high electric fields using full band structure, J. Appl. Phys. **95**, 4866 (2004).

[19] Y. Kamkura, T. Kotani, K. Konaga, N. Minamitani, G. Wakimura, and N. Mori, in *2016 International Conference on Simulation of Semiconductor Processes and Devices (SISPAD)*, SISPAD Proceedings, Vol. 2016 (Nuremberg, Germany, 2016), p. 47.

[20] P. Giannozzi, *et al.*, QUANTUM ESPRESSO: A modular and open-source software project for quantum simulations of materials, J. Phys. Condens. Matter **21**, 395502 (2009).

[21] P. Giannozzi, *et al.*, Advanced capabilities for materials modelling with QUANTUM ESPRESSO, J. Phys. Condens. Matter **29**, 465901 (2017).

[22] D. R. Hamann, Optimized norm-conserving Vanderbilt pseudopotentials, Phys. Rev. B **88**, 085117 (2013).

[23] M. Schlipf and F. Gygi, Optimization algorithm for the generation of ONCV pseudopotentials, Comput. Phys. Commun. **196**, 36 (2015).

[24] J. Heyd, G. E. Scuseria, and M. Ernzerhof, Hybrid functionals based on a screened Coulomb potential, J. Chem. Phys. **118**, 8207 (2003).

[25] J. Heyd, G. E. Scuseria, and M. Ernzerhof, Erratum: "Hybrid functionals based on a screened Coulomb potential" [J. Chem. Phys. 118, 8207 (2003)], J. Chem. Phys. **124**, 219906 (2006).

[26] O. Madelung, *Semiconductors: Data Handbook* (Springer, Berlin, 2004), 3rd ed.

[27] M. Grumet, P. Liu, M. Kaltak, J. Klimes, and G. Kresse, Beyond the quasiparticle approximation: Fully self-consistent GW calculations, Phys. Rev. B **98**, 155143 (2018).

[28] O. C. Zienkiewicz, R. L. Taylor, and J. Z. Zhu, *The Finite Element Method: Its Basis and Fundamentals* (Elsevier, London, UK, 2005).

[29] K. Hess, *Monte Carlo Device Simulation: Full Band and Beyond* (Springer Science & Business Media, New York, NY, 2012), Vol. 144.

[30] X. Gonze and C. Lee, Dynamical matrices, Born effective charges, dielectric permittivity tensors, and interatomic force constants from density-functional perturbation theory, Phys. Rev. B **55**, 10355 (1997).

[31] S. Baroni, S. de Gironcoli, A. Dal Corso, and P. Giannozzi, Phonons and related crystal properties from density-functional perturbation theory, Rev. Modern Phys. **73**, 515 (2001).

[32] J. P. Perdew, K. Burke, and M. Ernzerhof, Generalized gradient approximation made simple, Phys. Rev. Lett. **77**, 3865 (1996).

[33] S. Poncé, E. Margine, C. Verdi, and F. Giustino, EPW: Electron-phonon coupling, transport and superconducting properties using maximally localized Wannier functions, Comput. Phys. Commun. **209**, 116 (2016).

[34] G. Pizzi, *et al.*, WANNIER90 as a community code: New features and applications, J. Phys. Condens. Matter **32**, 165902 (2020).

[35] F. Giustino, M. L. Cohen, and S. G. Louie, Electron-phonon interaction using Wannier functions, Phys. Rev. B **76**, 165108 (2007).

[36] C. Jacoboni and P. Lugli, *The Monte Carlo Method for Semiconductor Device Simulation* (Springer Science & Business Media, Wien, 2012).

[37] E. O. Kane, Electron scattering by pair production in silicon, Phys. Rev. **159**, 624 (1967).

[38] M. V. Fischetti, N. Sano, S. E. Laux, and K. Natori, Full-band-structure theory of high-field transport and impact ionization of electrons and holes in Ge, Si, and GaAs, IEEE J. Technol. Aided Design, 1 (1996).

[39] T. Kunikiyo, M. Takenaka, M. Morifuji, K. Taniguchi, and C. Hamaguchi, A model of impact ionization due to the primary hole in silicon for a full band Monte Carlo simulation, J. Appl. Phys. **79**, 7718 (1996).

[40] N. Sano and A. Yoshii, Impact-ionization theory consistent with a realistic band structure of silicon, Phys. Rev. B **45**, 4171 (1992).

[41] F. Bertazzi, M. Moresco, and E. Bellotti, Theory of high field carrier transport and impact ionization in wurtzite GaN. Part I: A full band Monte Carlo model, J. Appl. Phys. **106**, 063718 (2009).

[42] I. Prigozhin, S. Dominici, and E. Bellotti, FBMC3D—A large-scale 3-D Monte Carlo simulation tool for modern electronic devices, IEEE Trans. Electron Devices **68**, 279 (2021).

[43] A. Portier, F. Donatini, D. Dauvergne, M.-L. Gallin-Martel, and J. Pernot, Carrier mobility up to $10^6$ $cm^2$ $V^{-1}$ $S^{-1}$ measured in single crystal diamond by the time of flight electron beam induced current technique, Phys. Rev. Appl. **20**, 024037 (2023).

[44] N. Sanders and E. Kioupakis, Phonon- and defect-limited electron and hole mobility of diamond and cubic boron nitride: A critical comparison, Appl. Phys. Lett. **119**, 062101 (2021).

[45] M. Katagiri, J. Isoya, S. Koizumi, and H. Kanda, Lightly phosphorus-doped homoepitaxial diamond films grown by chemical vapor deposition, Appl. Phys. Lett. **85**, 6365 (2004).

[46] H. Looi, R. Jackman, and J. S. Foord, High carrier mobility in polycrystalline thin film diamond, Appl. Phys. Lett. **72**, 353 (1998).

[47] F. Nava, C. Canali, M. Artuso, E. Gatti, P. F. Manfredi, and S. Zozlov, Transport properties of natural diamond used as nuclear particle detector for a wide temperature range, IEEE Trans. Nucl. Sci. **26**, 308 (1979).

[48] A. Hiraiwa and H. Kawarada, Figure of merit of diamond power devices based on accurately estimated impact ionization processes, J. Appl. Phys. **114**, 034506 (2013).

[49] A. Hiraiwa and H. Kawarada, Blocking characteristics of diamond junctions with a punchthrough design, J. Appl. Phys. **117**, 124503 (2015).

[50] J. Isberg, M. Gabrysch, A. Tajani, and D. Twitchen, High-field electrical transport in single crystal CVD diamond diodes, Adv. Sci. Technol. **48**, 73 (2006).

[51] K. Driche, H. Umezawa, N. Rouger, G. Chicot, and E. Gheeraert, Characterization of breakdown behavior of diamond Schottky barrier diodes using impact ionization coefficients, Jpn. J. Appl. Phys. **56**, 04CR12 (2017).

[52] S. Rashid, A. Tajani, D. Twitchen, L. Coulbeck, F. Udrea, T. Butler, N. Rupesinghe, M. Brezeanu, J. Isberg, A. Garraway, M. Dixon, R. Balmer, D. Chamund, P. Taylor, and G. A. J. Amaratunga, Numerical parameterization of chemical-vapor-deposited (CVD) single-crystal diamond for device simulation and analysis, IEEE Trans. Electron Devices **55**, 2744 (2008).

[53] T. Watanabe, M. Irie, T. Teraji, T. Ito, Y. Kamakura, and K. Taniguchi, Impact excitation of carriers in diamond under extremely high electric fields, Jpn. J. Appl. Phys. **40**, L715 (2001).

[54] K. Brennan, *The Physics of Semiconductors: With Applications to Optoelectronic Devices* (Cambridge University Press, Cambridge, UK, 1999).

[55] V. Mortet, N. Lamberst, P. Hubik, and A. Soltani, in *Proceedings 10th International Conference on Nanomaterials—Research & Application* (Brno, Czech Republic, 2018), p. 41.

[56] V. Mortet and A. Soltani, Impurity impact ionization avalanche in $p$-type diamond, Appl. Phys. Lett. **99**, 202105 (2011).

[57] O. Slobodyan, J. Flicker, J. Dickerson, J. Shoemaker, A. Binder, T. Smith, S. Goodnick, R. Kaplar, and M. Hollis, Analysis of the dependence of critical electric field on semiconductor bandgap, J. Mater. Res. **27**, 849 (2022).

[58] M. M. Hayat, W. L. Sargeant, and B. E. Saleh, Effect of dead space on gain and noise in Si and GaAs avalanche photodiodes, IEEE J. Quantum Electron. **28**, 1360 (1992).

[59] J. Yang, W. Huang, T. Chow, and J. Butler, High quality MPCVD epitaxial diamond film for power device application, MRS Online Proc. Library **829**, 29 (2004).

[60] J. Butler, M. Geis, K. Krohn, J. Lawless Jr, S. Deneault, T. Lyszczarz, D. Flechtner, and R. Wright, Exceptionally high voltage Schottky diamond diodes and low boron doping, Semicond. Sci. Technol. **18**, S67 (2003).

[61] Z. Han and C. Bayram, Diamond *p*-type lateral Schottky barrier diodes with high breakdown voltage (4612 V at 0.01 mA/mm), IEEE Electron Device Lett. **44**, 1692 (2023).

[62] T. Iwasaki, J. Yaita, H. Kato, T. Makino, M. Ogura, D. Takeuchi, H. Okushi, S. Yamasaki, and M. Hatano, 600 V diamond junction field-effect transistors operated at 200 °C, IEEE Electron Device Lett. **35**, 241 (2013).

[63] M. Landstrass, M. Plano, M. Moreno, S. McWilliams, L. Pan, D. Kania, and S. Han, Device properties of homoepitaxially grown diamond, Diam. Rel. Mat. **2**, 5 (1993).

[64] M. Moresco, F. Bertazzi, and E. Bellotti, GaN avalanche photodectors: A full band Monte Carlo study of gain, noise and bandwidth, IEEE J. Quantum Electron. **47**, 447 (2011).

[65] A. Selberherr, *Analysis and Simulation of Semiconductor Devices* (Springer-Verlag, Wien, 1984).

[66] C. Canali, G. Majni, R. Minder, and G. Ottaviani, Electron and hole drift velocity measurements in silicon and their empirical relation to electric field and temperature, IEEE Trans. Electron Devices **22**, 1045 (1975).